PNAS RESEARCH ARTICLE | CHEMISTRY

Dual-axial engineering on atomically dispersed catalysts for ultrastable oxygen reduction in acidic and alkaline solutions

Meng Dan[a,b], Xiting Zhang[a], Yongchao Yang[c], Jingfei Yang[a], Fengxiu Wu[a], Shenlong Zhao[c,1], and Zhao-Qing Liu[a,1]

Edited by Alexis Bell, University of California, Berkeley, CA; received October 18, 2023; accepted December 13, 2023

Atomically dispersed catalysts are a promising alternative to platinum group metal catalysts for catalyzing the oxygen reduction reaction (ORR), while limited durability during the electrocatalytic process severely restricts their practical application. Here, we report an atomically dispersed Co-doped carbon–nitrogen bilayer catalyst with unique dual-axial Co–C bonds (denoted as Co/DACN) by a smart phenyl-carbon-induced strategy, realizing highly efficient electrocatalytic ORR in both alkaline and acidic media. The corresponding half-wave potential for ORR is up to 0.85 and 0.77 V (vs. reversible hydrogen electrode (RHE)) in 0.5 M H_2SO_4 and 0.1 M KOH, respectively, representing the best ORR activity among all non-noble metal catalysts reported to date. Impressively, the Zn–air battery (ZAB) equipped with Co/DACN cathode achieves outstanding durability after 1,688 h operation at 10 mA cm^{-2} with a high current density (154.2 mA cm^{-2}) and a peak power density (210.1 mW cm^{-2}). Density functional theory calculations reveal that the unique dual-axial cross-linking Co–C bonds of Co/DACN significantly enhance the stability during ORR and also facilitate the 4e⁻ ORR pathway by forming a joint electron pool due to the improved interlayer electron mobility. We believe that axial engineering opens a broad avenue to develop high-performance heterogeneous electrocatalysts for advanced energy conversion and storage.

atomically dispersed catalyst | dual-axial cross-linking bonds | oxygen reduction reaction | joint electron pool | Zn–air battery

Significance

The single-atom catalysts (SACs) are currently the most promising low-cost catalysts for oxygen reduction reaction (ORR) in fuel cells and metal–air batteries. The superior activity is still the first impression when talking about SACs. However, stability is one of the most maligned aspects of SACs, that must be addressed, and only then can it truly become a substitute for platinum group metal (PGM) catalysts. We developed an atomically dispersed Co-doped carbon–nitrogen bilayer catalyst (Co/DACN) with unique dual-axial Co–C bonds by a phenyl-carbon-induced strategy, and in situ–generated metal–C axial ligand bond could favor electronic transfer of interlayers and significantly stabilized the SACs structure, which then significantly enhance 4e⁻ ORR activity and durability in both acidic and alkaline media.

The oxygen reduction reaction (ORR), involving multiple proton-coupled electron transfer (PCET) processes, plays a crucial role in many renewable energy storage systems, such as fuel cells and metal–air batteries (1–5). However, the sluggish kinetics of ORR due to the considerable overpotential of the four PCET processes seriously hinders the practical application of these sustainable technologies (6, 7). Generally, platinum-based catalysts are usually efficient for ORR, but their wider applications are restricted by the high price and low natural reserves (8–10). Note that noble metal–based catalysts often suffer from multiple other drawbacks, including low selectivity, poor durability, impurity poisoning, fuel cross-over effects, and detrimental effects on the environment. Therefore, the development of noble metal–free catalysts with low cost, high activity, and strong durability for ORR is thereby increasingly attractive but arduous with great challenges ahead.

Recently, single-atom catalysts (SACs) with the M–N_x–C (M stands for nonprecious metal elements) configuration exhibit superior ORR performance, owing to their ultrahigh metal utilization efficiency (~100%), unique local electronic structure, and tunable microenvironments of active centers (9, 11–15). However, the instability or poor robustness of SACs substantially stints their large-scale applications (16). In particular, atomically dispersed catalysts tend to be unstable during ORR because of the high surface free energy, which increases significantly with catalyst dispersion at the atomic level (16, 17) and leads to aggregation/dissolution of metal atoms (18, 19). Additionally, currently reported SACs usually feature monolayer structures with weak interlayered interactions, which is also responsible for the unsatisfactory stability of atomically dispersed catalysts under diverse reaction conditions. Thus, the development of high-performance SACs with remarkable stability for ORR is an urgent priority for commercial applications.

Designing bilayer SACs by interlayer axial bonds is regarded as a promising strategy for developing efficient and stable electrocatalysts because the existence of interlayer axial bonds can not only strengthen the interlayer interaction to improve the structural stability of SACs but also facilitate the interlayer electron conduction (20–26). Over the past few decades, numerous bilayer SACs have been reported for promoting ORR (20–23, 25–27). For example, Dai et al developed an in situ atomization of metal oxide nanoparticles strategy to synthesize sublayer Fe–N_x–C with interlayer metal–metal (Fe-Fe) axial bonds in 2022 (21). Accordingly, the sublayer-enhanced SACs obtained an optimum activity for the ORR, significantly higher performance in comparison to that of single-layer SACs. However, for the monoaxial bilayer catalysts reported thus far, the incorporation of reactive

Author contributions: S.Z. and Z.-Q.L. designed research; M.D. and X.Z. performed research; M.D., X.Z., Y.Y., and F.W. contributed new reagents/analytic tools; M.D., X.Z., Y.Y., J.Y., F.W., S.Z., and Z.-Q.L. analyzed data; and M.D., Y.Y., J.Y., S.Z., and Z.-Q.L. wrote the paper.

The authors declare no competing interest.

This article is a PNAS Direct Submission.

[1]To whom correspondence may be addressed. Email: shenlong.zhao@sydney.edu.au or lzqgzu@gzhu.edu.cn.

This article contains supporting information online at https://www.pnas.org/lookup/suppl/doi:10.1073/pnas.2318174121/-/DCSupplemental.

Published January 30, 2024.

species is likely to induce the rupture of interlayer axial bonds, leading to the collapse/aggregation of the as-formed low-stability structures during the reaction (28, 29). Accordingly, addressing the stability issue of bilayer SACs during ORR is highly desired while remaining exceedingly challenging.

Herein, we develop Co/DACN as a bilayer SAC induced by phenyl carbons. The dual-axial bonds are composed of uncovered Co (layer 1)–C (layer 2) and Co (layer 2)–C (layer 1) to cross-link two layers, which are distinct from traditional metal–metal bonds (30, 31) or metal–X–metal bonds (X: exo-ligand) (23, 28, 29) to link two layers. Systematic experimental results and theoretical calculations reveal that the dual-axial cross-linking bonds significantly enhance the stability of the SACs structure during the ORR process, far outperforming all other reported SACs. Furthermore, this new-type axial Co–C bond facilitates the interlayer electron transfer to form a collective electron pool, simultaneously accelerating the $4e^-$ ORR process. Therefore, Co/DACN electrocatalyst affords remarkable ORR activity and stability in both acidic and alkaline media (i.e., pH-universal solutions). This work provides an inspiring strategy to develop PGM (platinum group metal)-free electrocatalysts with high ORR reactivity and stability by designing interlayer dual-axial structures.

Results and Discussion

Electrocatalyst Synthesis and Characterization. The synthesis of Co/DACN involved a facile two-step process, as illustrated in Fig. 1*A*. First, a simple solvothermal treatment was used to obtain the Co-ZIF-8. Compared with ZIF-8, Co-ZIF-8 displayed a similar morphology with typical rhombic dodecahedron crystals of ca. 200 nm (*SI Appendix*, Fig. S1) and an almost unaltered X-ray diffraction (XRD) diffraction pattern (*SI Appendix*, Fig. S2), indicating that the introduction of Co did not change the geometric structure and crystal structure of ZIF-8. And then, using the as-obtained Co-ZIF-8 as a precursor, Co/CN and Co/DACN were prepared by a pyrolysis process at 900 °C and 950 °C, respectively.

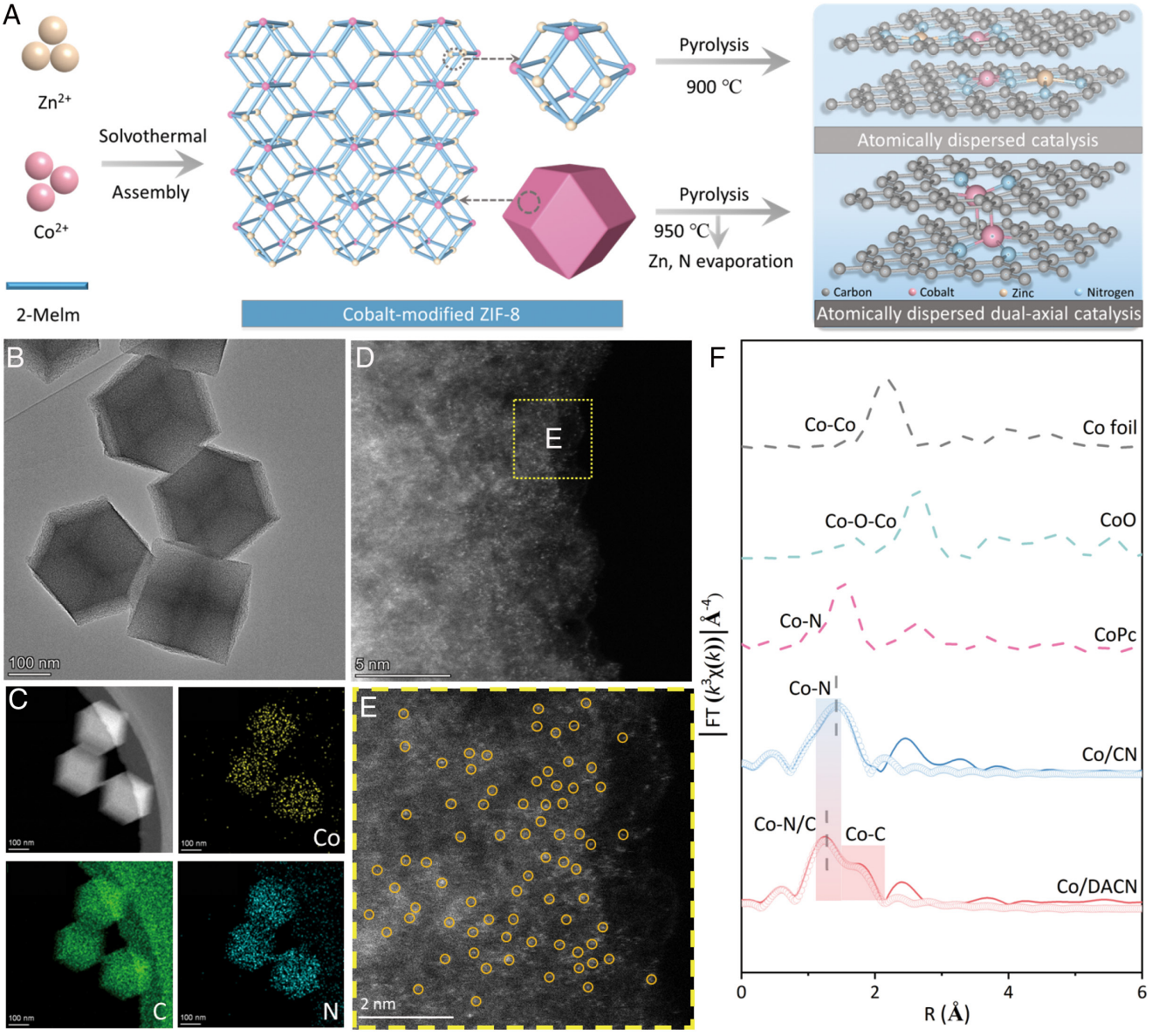

Fig. 1. Synthesis and structural characterizations of Co/DACN. (*A*) Schematic illustration for the synthesis. (*B*) HAADF-STEM images. (*C*) STEM image and corresponding elemental distributions of Co (yellow), C (green), and N (blue). (*D* and *E*) High-resolution HAADF-STEM images. (*F*) FT-EXAFS spectra and corresponding fitting curves at Co K-edge for Co/CN, Co/DACN, and reference samples.

"CN" stands for N-doped carbon matrix obtained from the carbonization of 2-methylimidazole (mIm) during pyrolysis. For comparison, monometallic Zn/CN was also prepared by pyrolysis of ZIF-8 at 900 °C. All metal/CN samples, including Zn/CN, Co/CN, and Co/DACN, exhibited similar XRD patterns with only two broad peaks located near 25° and 44°, which are attributed to the characteristic diffractions of graphitic carbon (*SI Appendix*, Fig. S3) (32–34). This result indicates that ZIFs (ZIF-8 and Co-ZIF-8) were successfully carbonized, further supported by G-band peaks in the Raman spectrum (*SI Appendix*, Fig. S4). Moreover, no signal of metal nanoparticles or any other metal-containing phase was observed in the XRD patterns (*SI Appendix*, Fig. S3), demonstrating that no obvious aggregation of metal (Zn or Co) species occurred in the above-prepared samples. After thermal treatment, all metal/CN samples could also maintain the initial rhombic dodecahedron shape (*SI Appendix*, Fig. S5).

Further, high-angle annular dark-field scanning transmission electron microscopy (HAADF-STEM) was employed to characterize the dispersion and shape of all metal–CN samples (Fig. 1 and *SI Appendix*, Figs. S6 and S7). First, all samples showed a similar dodecahedron shape with no observable metal nanoparticles (Fig. 1*B* and *SI Appendix*, Figs. S6*A* and S7*B*). The corresponding energy-dispersive X-ray elemental mapping results demonstrated that Co, Zn, N, and C were homogeneously distributed over all samples (Fig. 1*C* and *SI Appendix*, Figs. S6*D* and S7*D*). The individual bright dots (highlighted by yellow circles) obviously exhibited the atomic dispersion of metal sides on all samples (Zn/CN, Co/CN, and Co/DACN) using a high-resolution HAADF-STEM (Fig. 1 *D* and *E* and *SI Appendix*, Figs. S6 *B* and *C* and S7 *B* and *C*). Subsequently, the actual loading of metal sites was calculated by inductively coupled plasma atomic emission spectroscopy, as presented in *SI Appendix* (*SI Appendix*, Table S1). In addition, the atomic ratio of C/N and the chemical states of C, N, Zn, and Co in all samples were detected by the XPS test (*SI Appendix*, Figs. S8 and S9 and Table S2). Co/DACN showed a larger C/N ratio (29.53) than that of Co/CN (7.08) (*SI Appendix*, Table S2), which may be beneficial to the formation of phenyl carbons.

Coordination Environment Analysis of Co/DACN. X-ray absorption near edge structure (XANES) and extended X-ray absorption fine structure (EXAFS) were performed to further elucidate the chemical states and coordination environments of metal species throughout the SACs. Co K-edge XANES spectra of Co/CN and Co/DACN were illustrated to confirm that the valence state of Co was close to +2 (*SI Appendix*, Fig. S10*A* and Tables S3–S5). The FT-EXAFS spectra of Co foil and CoO revealed Co–Co and Co–O–Co signals at 2.2 Å and 2.6 Å, respectively (Fig. 1*F*). However, no such signal was found for Co/CN and Co/DACN (see FT-EXAFS spectra in Fig. 1*F*). The FT-EXAFS curve of Co/CN showed a prominent peak at around 1.45 Å, which was similar to that (1.51 Å) in cobalt phthalocyanine (CoPc) catalysts (35–37), assigned to the first shell Co–N scattering path. However, an additional shoulder FT-EXAFS peak was observed at about 1.74 Å for Co/DACN, which was different from that of Co/CN or CoPc (Fig. 1*F*). Further, the FT-EXAFS curve of Co/DACN exhibited a prominent peak at around 1.27 Å (Fig. 1*F*). These results illustrated that the coordination environment of Co in Co/DACN and Co/CN was different. The contour maximum of k in WT EXAFS spectra was different from that of Co foil but similar to CoPc, thereby strongly proving that Co was atomically dispersed in Co/CN and Co/DACN (*SI Appendix*, Fig. S10*B*). In addition, the K-edge XANES spectra of Zn (*SI Appendix*, Fig. S11) in Co/CN were also investigated, indicating that the coordination environment of Zn in Co/CN was identical to that of zinc phthalocyanine and reference Zn/CN. This result confirmed the weak interactions between Zn and Co in Co/CN, suggesting that a small amount of Zn (~5.04 wt.%) has a negligible effect on the catalytic performance (38). Certainly, the as-obtained Co/CN with porphyrin-like structure (MN_4) can act as a reference sample (33).

In light of the above XANES and EXAFS results, Co was atomically dispersed in Co/CN and Co/DACN. Furthermore, the k-space oscillation was converted from the energy space oscillation (*SI Appendix*, Figs. S12 and S13) with the *R* space data extracted through the Fourier transform, providing a basis for fitting the bond length and the coordination number (*SI Appendix*, Table S6). Therefrom, the first shell of the central atom Co of Co/CN displayed a coordination number of 4 (*SI Appendix*, Table S6), directly connected by four N atoms, which is similar to CoPc. Notably, the first shell of the central atom Co of Co/DACN might showcase a coordination structure with a coordination number of 5, directly connected by two N atoms and three C atoms. This result directly verified that Co/DACN possessed different coordination environments.

The Co–C_3N_2 moieties intimated a possible change in electronic structure from the commonly accepted monolayer of M–N_4 SACs to the bilayer of Co/DACN. Co/DACN affords uniformly dispersed Co–C_2N_2 active sites derived from two phenyl C atoms and two pyridine N atoms. The phenyl carbon exhibited carbene character, leading to the formation of the Π_6^5 phenyl group, which is electron-deficient and unstable compared with the Π_6^6 pyridine group (Fig. 2*A*). On the other hand, Co(II) had a d^7 electron configuration. Therefore, the Π_6^5 phenyl carbon atom in the first layer can act as the axial ligand coordinated to Co (d^7) in the second layer. Meanwhile, the Co (d^7) active site in the first layer also can be anchored on the Π_6^5 phenyl carbon atom in the second layer. The dual-axial cross-linking bonds were then formed and could be expected to significantly stabilize the Π_6^5 phenyl group and the d^7 Co center, which can be further supported by density functional theory (DFT) calculation for structural optimization (Fig. 2 *B* and *C*). This is why Co/DACN possessed Co–C_3N_2 moieties instead of Co–C_2N_2 ones. The Co–N_4 from Co/CN did not have dual-axial Co–N bonds cross-linking the two layers since the Π_6^6 pyridine nitrogen was not conducive to an effective ligand bonding to the d^7 Co site. To verify the unique dual-axial configuration, we further performed the XANES calculation (Fig. 2*D*), whose result was in good agreement with our experimental data acquired for Co/DACN catalysts, thus revealing that we successfully obtained the dual-axial Co–C bonds cross-linking bilayer catalysts with Co–C_3N_2 moieties. Meantime, the prominent peak of Co/DACN at around 1.27 Å can be attributed to the equatorial plane Co–C and Co–N (Fig. 2*D*). The isolated M–N_5 sites with monoaxial pyridine N atoms have recently been reported to construct bilayer catalysts (21, 22, 37, 39–41). Traditional metal–metal bonds (30, 31) or metal–X–metal bonds (X: exo-ligand) (23, 29) can also be used to build bilayer catalysts. However, we have identified dual-axial cross-linking bonds, which can be predicted to be more stable than the monoaxial bond for the bilayer catalyst. Furthermore, the interconnected network bilayer structure is able to provide effective channels for electron transmission/fluxion, which is favorable for the formation of joint electron pools (42). Based on the above XANES, EXAFS, and DFT results, Co/DACN catalysts with unique dual-axial microstructures were successfully constructed.

Electronic Structure and Reaction Process Analysis of Co/DACN. Motivated by the above discussion, we further conducted DFT calculations to investigate the influence of the unique dual-axial

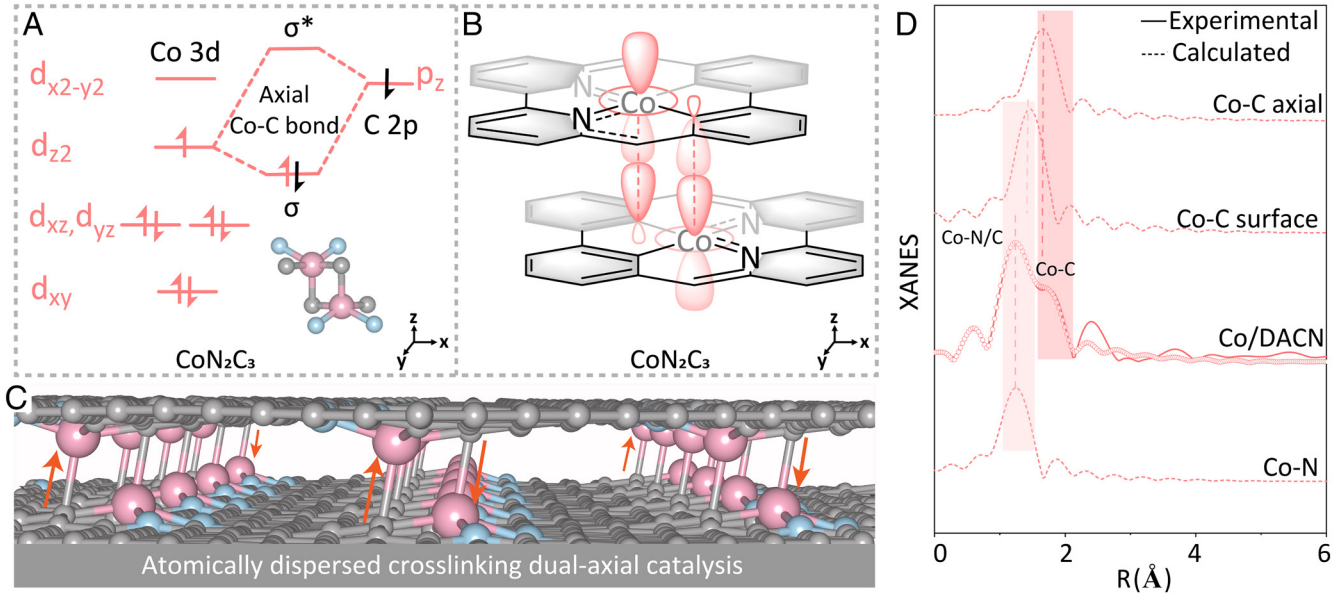

Fig. 2. Structural analysis and possible formation and reaction mechanism. (*A*) Co 3d electron and d-orbital of CoN_2C_3 configuration. (*B*) The formation mechanism of Co/DACN with dual-axial electronic transfer channel. (*C*) Experimental and fitted XANES spectra at Co K-edge of Co/CN and Co/DACN. (*D*) Optimized structure models of Co/DACN.

microstructure introduced into the Co/DACN toward the ORR pathway. The structure models were judiciously constructed according to the above EXAFS fitting (*SI Appendix*, Figs. S14 and S15). And the total density of states was first displayed (*SI Appendix*, Fig. S16). It was found that the electronic states were distributed across the Fermi level for all systems, proving outstanding electronic conductivity for electron transmission (43). Additionally, Co orbitals exhibited the highest occupied states near the Fermi level. They were closely linked with the electronic interactions between adsorbates and catalysis surfaces. The partial densities of state (pDOS) for Co-3d orbitals in Co/CN and Co/DACN catalysts were calculated. In contrast to Co/CN, the states of the Co-3d orbital of Co/DACN were delocalized, as indicated by the splitting of the pDOS peaks (*SI Appendix*, Fig. S17). Thus, it was favorable to the desorption of O-containing intermediates. Generally, the interaction between metal and intermediates was considered the coupling between the valence states of intermediates and the d states of metal, inducing the formation of bonding and antibonding states (44–46). Accordingly, the d-band center (E_d) energy levels of different catalysts were calculated. As displayed in *SI Appendix* (*SI Appendix*, Fig. S18), the d-band center of the Co atom in Co/DACN possessed lower E_d energy levels (−1.03 eV) than Co/CN (−0.84 eV), suggesting that the antibonding energy states were lowered and easy to be filled, thus reducing the Co–O_2 π backdonation and enabling the rapid desorption of ORR intermediates (44–47). Moreover, we builded the monolayer Co/DACN structure (Co/DACN-S) to study the functionality of dual-axial cross-linking Co–C structure (*SI Appendix*, Fig. S15). Accordingly, the enhanced −0.32 eV of the d-band center in Co/DACN-S could lead to the strong affinity that enabled the intermediates difficult to desorb, indicating that the existence of interlayer Co–C played a crucial role in promoting the Co band widening to lower the position of d band center. The electron location function map of Co/DACN showed that the joint electron pool arose by electron delocalization (*SI Appendix*, Fig. S19), originating from interconnected dual-axial Co–C bonds in Co/DACN, which is consistent with the differential charge density mappings (*SI Appendix*, Fig. S19). And the XPS test results further verified this point. The Co $2p_{3/2}$ in Co/DACN possessed higher binding energy (780.88 eV) than Co/CN (780.45 eV, *SI Appendix*, Fig. S20), indicating that Co sites in Co/DACN structure can capture fewer electrons compared to Co/CN. These results demonstrated that more electrons could be delocalized in Co/DACN. Certainly, the joint electron pool originating from the delocalized electronic structure showed an amazing "self-adjustment" ability to regulate the charge distribution in multiple PCET processes, resulting in excellent electrocatalytic activities (42).

Next, we also calculated the reaction energies of ORR elementary steps on each site at different U values (0, 0.85, 1.23 V). The equatorial plane Co–C could promote *OOH dissociation (*OOH → *O), while the axial Co–C was favorable for *OH desorption. In addition, the most endothermic step for Zn/CN was the second step of breaking *OOH (*SI Appendix*, Figs. S21 and S22), which tended to the $2e^-$ ORR process. The above results vividly proved that the joint electron pool in Co/DACN could synergistically modulate multiple PCET processes. Therefore, based on the above DFT and experimental data, we predicted that Co/DACN displayed remarkable ORR activity.

ORR Electrocatalytic Activity. Inspired by the above predictions, the electrocatalytic ORR performance of as-synthesized catalysts was first evaluated using a rotating ring-disk electrode in a 0.1 M KOH electrolyte. Cyclic voltammetry measurements of Co/DACN were performed in O_2- or N_2-saturated electrolytes, and a well-defined cathodic peak was clearly observed in the O_2-saturated solution (*SI Appendix*, Fig. S23), indicating that the sample had ORR activities. Linear scanning voltammetry (LSV) curves obtained at a rotation speed of 1,600 rpm and a scan rate of 10 mV s^{-1} revealed the best ORR performance of Co/DACN among all tested catalysts (Fig. 3*A*). Furthermore, the Tafel slope value of Co/DACN (73 mV dec^{-1}) was the lowest among all samples (Pt/C: 76, Co/CN: 88 and Zn/CN: 115 mV dec^{-1}), demonstrating the fastest reaction kinetics (Fig. 3*B*). Correspondingly, LSV analysis results (Fig. 3*C* and *SI Appendix*, Table S7) showed that Co/DACN catalyst offered an onset potential of 0.95 V (at 0.1 mA cm^{-2}), a

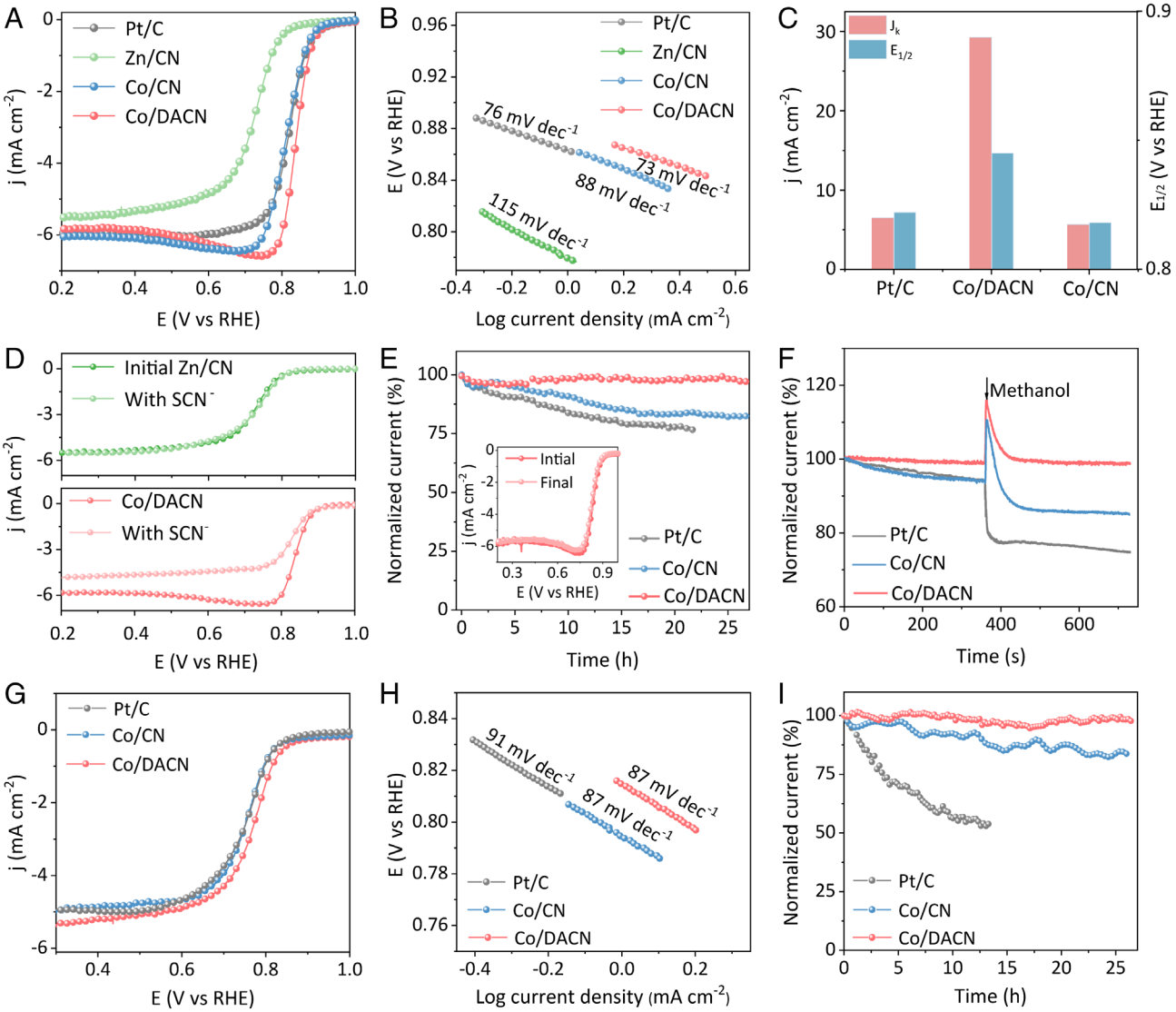

Fig. 3. ORR performance. Alkaline condition (0.1 M KOH): (*A*) ORR LSV curves in O_2-saturated 0.1 M KOH solution at a scan rate of 10 mV s^{-1} and a rotation rate of 1,600 rpm. (*B*) The corresponding Tafel plots. (*C*) Half-wave potential $E_{1/2}$ and kinetic current density J_k for different catalysts. (*D*) Steady-state ORR polarization curves recorded in O_2-saturated 0.1 M KOH with or without poisoning by 0.01 M SCN^- at a scan rate of 10 mV s^{-1} and a rotation rate of 1,600 rpm. (*E*) CA test of the catalysts at 0.6 V (vs. RHE) and a rotation rate of 1,600 rpm in O_2-saturated 0.1 M KOH solution. (*F*) Methanol tolerance test at 0.85 V (vs. RHE) and a rotation rate of 1,600 rpm in O_2-saturated 0.1 M KOH solution containing 5 wt.% methanol; acidic condition (0.5 M H_2SO_4): (*G*) ORR LSV curves in O_2-saturated 0.5 M H_2SO_4 solution at a scan rate of 10 mV s^{-1} and a rotation rate of 1,600 rpm. (*H*) The corresponding Tafel plots. (*I*) CA test of the catalysts at 0.6 V (vs. RHE) and a rotation rate of 1,600 rpm in O_2-saturated 0.5 M H_2SO_4 solution.

half-wave potential ($E_{1/2}$) of 0.85 V, and a diffusion-limited current density of 5.84 mA cm^{-2} (at 0.2 V). Notably, Co/DACN exhibited significantly higher performance than traditional Co/CN ($E_{1/2}$: 0.82 V) and commercial 20 wt.% Pt/C ($E_{1/2}$: 0.82 V). The kinetic current density (J_k) analysis presented a similar result to $E_{1/2}$, and the highest J_k value of Co/DACN further verified its remarkable ORR performance over Pt/C and Co/CN samples (Fig. 3*C*). Additionally, Co/DACN also delivered a much higher mass and specific activity (*SI Appendix*, Fig. S24), which is about fivefold greater than that of Co/CN. Then, electrochemically active surface areas of all the as-obtained catalysts were measured by the non-Faradaic double-layer capacitance (C_{dl}). Distinctly, Co/DACN exhibited the highest C_{dl} (4.3 mF cm^{-2}) compared with those of Pt/C (3.6 mF cm^{-2}) and Co/CN (4.1 mF cm^{-2}) (*SI Appendix*, Figs. S25 and S26). Reasonably, a larger C_{dl} indicated that more electroactive sites existed in Co/DACN catalysts, bringing about superior ORR performance. This originated from the fact that the dual-axial cross-linking Co–C bonds can act as interlayer pillaring to modulate the pore structure (*SI Appendix*, Figs. S27 and S28 and Table S8), and the evaporation of Zn can induce the production of micropores, thereby increasing the surface area of Co/DACN catalyst (1,187.94 $m^2 g^{-1}$) (38).

And the electron transfer numbers (n) and H_2O_2 yield (H_2O_2%) of Co/DACN were also determined as about 4 and below 10%, respectively, confirming a direct $4e^-$ pathway (*SI Appendix*, Fig. S29). Then, thiocyanide (SCN^-) ions were introduced to determine the effect of Zn and Co atoms on ORR catalytic activity (Fig. 3*D*). The result showed that the ORR catalytic activity of Co/DACN was significantly inhibited. Notably, there was hardly any change in the ORR performance of Zn/CN, suggesting that Co atoms were the main active sites for $4e^-$ ORR in Co/CN and Co/DACN. Consequently, Co/DANC with unique cross-linking dual-axial microstructures was energetically more favorable for ORR than traditional Co/CN with porphyrin-like structures ($M–N_4$).

Considering the stringent requirements of ORR electrocatalysts for practical application in batteries, the stability of Co/DACN was

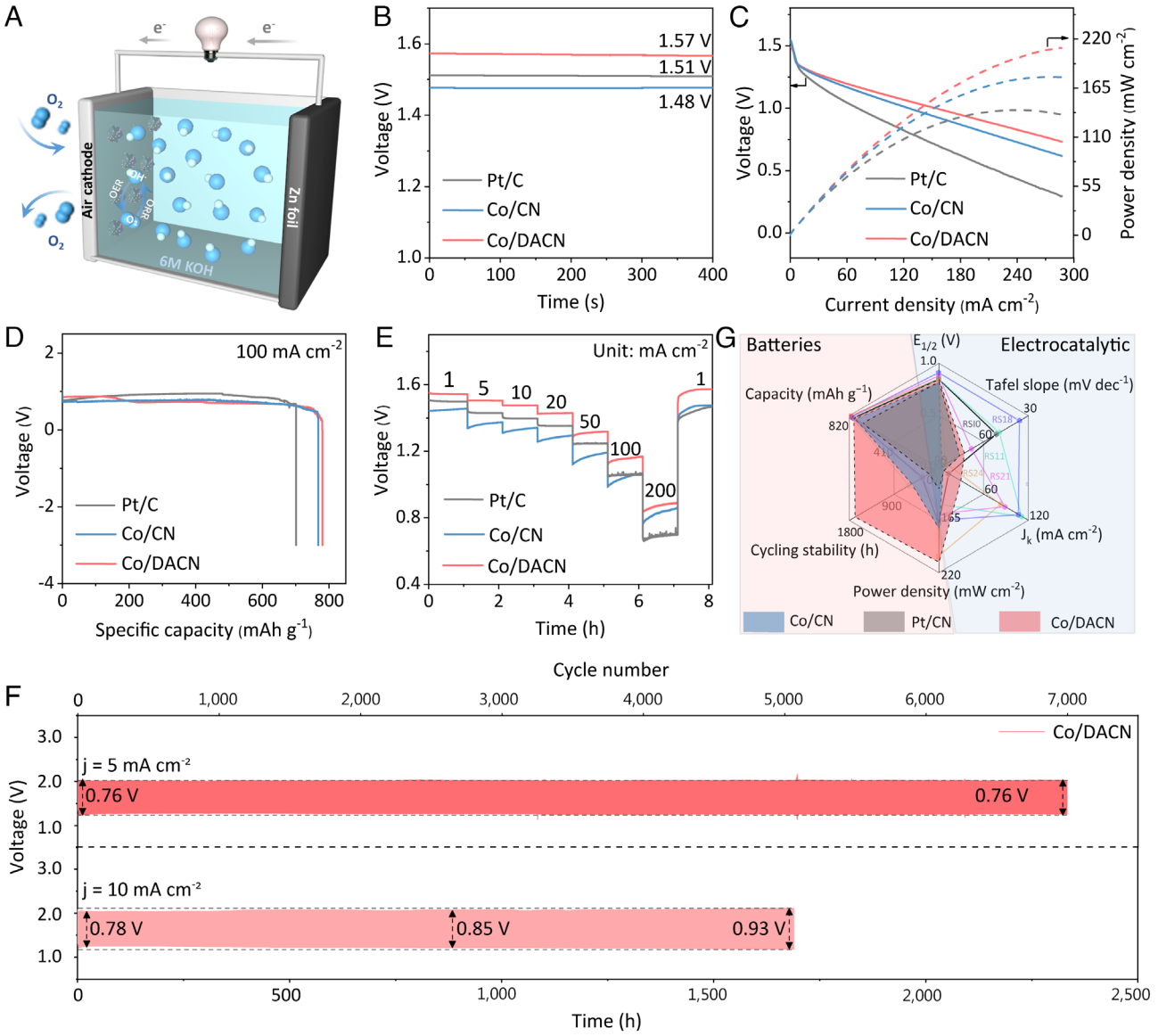

Fig. 4. Zn–air battery (ZAB) performance. (*A*) Schematic of the rechargeable ZAB. (*B*) Open-circuit plots of Zn–air battery tests. (*C*) Charge/discharge polarization profiles and power density curves of the ZABs. (*D*) Long-time galvanostatic discharge curves of the ZABs at 100 mA cm^{-2}. (*E*) Galvanostatic discharge curves of the Zn–air battery at different current densities. (*F*) Cycling performance with Co/DANC as the ORR catalyst and IrO_2 as the oxygen evolution reaction catalyst at 5 and 10 mA cm^{-2}. (*G*) Radar chart related comparing the ORR and ZAB performance (ORR: $E_{1/2}$, Tafel slope, and J_k; ZAB: capacity, power density, and cycling stability) of Co/DANC and reported state-of-the-art catalysts.

systematically investigated. First, the chronoamperometry (CA) measurement was employed (Fig. 3*E*). After 26 h, Co/DACN still retained 98.0% of the initial current with negligible loss in ORR performance (*Inset* of Fig. 3*E*), significantly higher than the retention rate of traditional Co/CN with MN_4 structure (82.5%) under the same conditions. Commercial Pt/C catalyst only retained 76.6% of the initial current after 21 h of continuous operation. In addition, the XRD results support the structural maintenance of Co/DACN after the ORR (*SI Appendix*, Fig. S30). The resistance to methanol cross-over was explored by injecting 5% (v/v) methanol into the electrolyte during the CA measurement. As shown in Fig. 3*F*, a significant current drop was observed for commercial Pt/C (~25%) and Co/CN (~15%), whereas Co/DACN only exhibited a negligible current density decay, demonstrating the high tolerance of Co/DACN to methanol cross-over effects.

And then, the ORR performance of Co/DACN in a more challenging acidic condition (0.5 M H_2SO_4) was also investigated (Fig. 3 *G–I*). The ORR activity with an $E_{1/2}$ of 0.77 V for Co/DACN was much higher than that of traditional Co/CN (0.75 V) and commercial Pt/C (0.76 V) (Fig. 3*G*). Co/DACN also exhibited a lower Tafel slope of 87 mV dec^{-1} than that of commercial Pt/C (91 mV dec^{-1}), suggesting favorable ORR kinetics (Fig. 3*H*). Similarly, CA measurement was also employed to evaluate the stability of Co/DACN in acidic media (Fig. 3*I*). After 26 h, Co/DACN still retained 97.8% of the initial current, significantly higher than that of Co/CN (82.5%) under the same conditions. The commercial Pt/C catalyst retained only 54.0% of the initial current after 13 h of continuous operation. From these results, it can be inferred that Co/DACN with unique dual-axial cross-linking Co–C covalent is a promising candidate for ORR in both alkaline and acidic electrolytes.

Zn–Air Battery (ZAB) Performance. The remarkable ORR activity and superior durability of Co/DACN catalysts greatly encouraged us to explore its practical application in energy devices. ZABs were constructed using Zn foil as anode and Co/DACN as air cathode in a 6 M KOH electrolyte for comparative performance evaluation (Fig. 4*A*). The ZAB with Co/DACN showed a high and stable open circuit voltage (OCV) of about 1.57 V (Fig. 4*B*), higher than

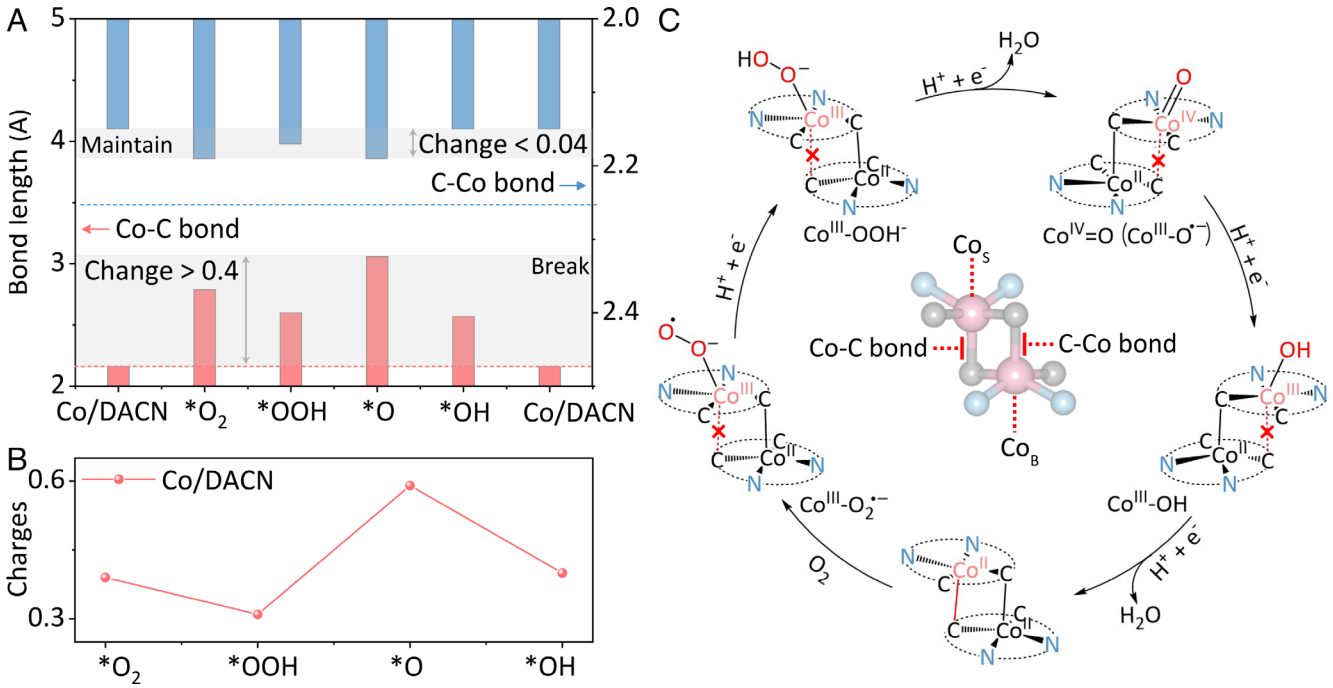

Fig. 5. Mechanism of excellent stability. (*A*) The Co–C (C–Co) bond length change in Co/DACN during ORR. (*B*) Charge transfer from Co sites to O intermediates. (*C*) 4e$^-$ ORR process on the Co–Co dinuclear site in the Co/DACN.

that of Co/CN (1.48 V) and commercial Pt/C (1.51 V), which is approaching to the theoretical threshold of ZABs (1.65 V). The charge/discharge polarization curves and the corresponding power density of ZABs are presented (Fig. 4*C* and *SI Appendix*, Fig. S31). Remarkably, at a voltage of 1.0 V, Co/DACN exhibited a high current density of 154.2 mA cm^{-2} and a maximum power density of 210.1 mW cm^{-2}, which is much higher than those of traditional Co/CN with MN_4 structure (123.6 mA cm^{-2} and 177.7 mW cm^{-2}) and commercial Pt/C (71.7 mA cm^{-2} and 140.4 mW cm^{-2}). Furthermore, Fig. 4*D* shows the galvanostatic discharge curves of Co/DACN-, Co/CN-, and Pt/C- driven batteries at a constant current density of 100 mA cm^{-2}. By normalizing with respect to the mass of consumed Zn, the specific capacity of Co/DACN-based ZAB was calculated to be 780 mAh g^{-1} (coulombic efficiency: 95.1% of the theoretical capacity, 820 mAh g^{-1}) (48, 49), which was superior to that of traditional Co/CN-based (767 mAh g^{-1}) and commercial Pt/C-based batteries (701 mAh g^{-1}). The Co/DACN-based battery with excellent rate capability and fast-dynamic response was also demonstrated (Fig. 4*E*); specifically, with the current density being decreased back again, the OCV value could recover without a detectable decrease for the Co/DACN-based battery. Meanwhile, the galvanostatic discharge curves of devices equipped with Co/DACN demonstrated excellent discharge stability at various current densities ranging from 1 to 200 mA cm^{-2} (Fig. 4*E*). Such impressive performance once again highlighted the superior catalytic activity and stability of Co/DACN catalysts for ORR.

To investigate the cycling stability, we conducted galvanostatic charge and discharge measurements (Fig. 4*F*). Co/DACN-based ZAB showed good cycling stability, even under the charge/discharge cycling test at 5 mA cm^{-2} (voltage gap: 0.76 V) beyond 2,336 h (> 7000 cycles) and at 10 mA cm^{-2} (voltage gap: 0.78 to 0.93 V) beyond 1,688 h (>5,000 cycles), with no significant change in potential difference. Such excellent cycling stability did outperform all reported electrocatalysts for ZABs to date under comparable conditions, including conventional Co/CN (<550 h, *SI Appendix*, Fig. S32) and commercial Pt/C (<200 h, *SI Appendix*, Fig. S33). The ORR and ZAB performances of Co/DACN were illustrated in the radar plot for comparison with other state-of-the-art SACs (Fig. 4*G*). Although previously reported SACs realized excellent ORR performance beyond Co/DACN, Co/DACN-based ZABs delivered an optimized performance in terms of stability and power density among state-of-the-art catalysts for ZABs (*SI Appendix*, Fig. S34 and Table S9). Therefore, SACs with unique dual-axial coordination structures enable ultrastable metal–air battery applications.

Stabilization Mechanism Analysis of Co/DACN. To thoroughly understand the enhanced ORR stability of Co/DACN. The corresponding atomic configuration details of Co/DACN for ORR were presented (*SI Appendix*, Fig. S35). The bond length of the dual-axial Co–C bonds changed significantly in this process. One Co–C bond (Co from surface, C from bulk) increased (Fig. 5*A*) since O-containing species (*O_2, *OOH, *O, and *OH) could extract electrons from Co sites, which disfavored axial Co–C bond formation in the ORR process. However, the other C–Co bond (C from surface, Co from bulk) could be maintained during the whole ORR process. For the monoaxial bilayer catalysts reported thus far, the incorporation of reactive species is able to induce the breaking of interlayer axial bonds, leading to a low-stability structure with collapse/aggregation in the reaction process (28, 29). Usually, the bond length change is directly related to charge distribution. Therefore, the differential charge densities and the corresponding Bader charge analysis were performed (Fig. 5*B* and *SI Appendix*, Fig. S36). Accordingly, the regularity of electron capture by O intermediates from Co sites was consistent with the change of Co–C bond lengths during ORR. Concretely, more electrons were needed to induce O-activation (*O_2, *O), and the O-protonation process (O_2 + (H^+ + e^-) → *OOH, and *O + (H^+ + e^-) → *OH) could inject external electrons by the electric field, which was favorable to reduce the charge capture from Co sites.

Based on the above bond length and charge distribution analysis results, the process of Co/DACN-catalyzed 4e$^-$ ORR was proposed (Fig. 5*C*). The 4e$^-$ ORR process was a multistep reaction, several of which could show a 4 (H^+ + e^-) PCET process: First, Co/DACN and O_2 molecules interacted to form a metal–superoxo intermediate (Co^{III}–$O_2^{\bullet-}$), and then the protonation of Co–$O_2^{\bullet-}$ adduct to yield

Co^{III}–OOH^- species, followed by the cleavage of the distal of Co^{III}–OOH^- to yield Co^{IV}=O (tautomeric forms: Co^{III}–$O^{\cdot-}$) species and one H_2O molecule. Finally, Co^{III}–OH was formed and further converted to an H_2O molecule by two steps, coupled with the H^+ and e^- ($H^+ + e^-$) process. This result verified that dual-axial cross-linking bonds play an important role in maintaining superior structural stability during ORR, preventing structure from collapse/aggregation. Therefore, developing SACs with dual-axial cross-linking bonds is of great importance for durable catalysts for various reaction processes.

Conclusions

In summary, we have successfully developed a Co/DACN catalyst with a unique cross-linking dual-axial structure by an ingenious phenyl-carbon-induced strategy. Systematic experimental results and theoretical calculations reveal that the in situ–generated bidirectional C–metal axial ligand bond manages to facilitate the electronic transfer of interlayers and drastically stabilize the structure of SACs, further significantly enhancing $4e^-$ ORR activity and durability in both acidic and alkaline media. These results have fundamental and significant implications for the understanding of the $4e^-$ ORR process and the design of SACs for the in situ–generated C–metal dual-axial bonds in bilayers and their potential applications in PGM-free catalysts.

Materials and Methods

The Co/DACN is synthesized by a facile two-step process; more details are provided in *SI Appendix*, *Experimental details* section. Characterization data include SEM images (*SI Appendix*, Figs. S1 and S5), XRD patterns (*SI Appendix*, Figs. S2, S3, and S30), Raman spectra (*SI Appendix*, Fig. S4), TEM and STEM images (*SI Appendix*, Figs. S6 and S7), XPS spectra (*SI Appendix*, Figs. S8, S9, and S20 and Tables S2–S5), XANES and EXAFS spectra (*SI Appendix*, Figs. S10–S13 and Table S6), DFT calculation (*SI Appendix*, Figs. S14–S19, S21, S22, S35, and S36), additional reaction data (*SI Appendix*, Figs. S23–S26 and S29) and Zn–air batteries (ZAB) performance (*SI Appendix*, Figs. S31–S34 and Tables S7 and S9), N_2 adsorption–desorption isotherms (*SI Appendix*, Figs. S27 and S28 and Table S8), ICP-MS (*SI Appendix*, Table S1) are included and described in *SI Appendix*.

Data, Materials, and Software Availability. All study data are included in the article and/or *SI Appendix*.

ACKNOWLEDGMENTS. This work was financially supported by the National Natural Science Foundation of China (Grant Nos. 22278094 and 22209029), Outstanding Youth Project of Guangdong Natural Science Foundation (2020B1515020028), China Postdoctoral Science Foundation (Grant No. 2021M700917), Guangdong Natural Science Foundation (No. 2022A1515011775), Guangdong Graduate Education Innovation Program (No. 2023JGXM_102), University Innovation Team Scientific Research Project of Guangzhou Education Bureau (No. 202235246), and Opening Fund of Key Laboratory for Water Quality and Conservation of the Pearl River Delta (Guangzhou University: KLWQCPRD-202301).

Author affiliations: [a]School of Chemistry and Chemical Engineering/Institute of Clean Energy Materials/Guangzhou Key Laboratory for Clean Energy and Materials/Key Laboratory for Water Quality and Conservation of the Pearl River Delta, Ministry of Education, Guangzhou University, Guangzhou 510006, People's Republic of China; [b]College of Materials Science & Engineering, Taiyuan University of Technology, Shanxi 030024, People's Republic of China; and [c]School of Chemical and Biomolecular Engineering, The University of Sydney, Sydney, NSW 2006, Australia

1. L. Schwiedrzik, V. Brieskorn, L. González, Flexibility enhances reactivity: Redox isomerism and jahn–teller effects in a bioinspired Mn_4O_4 cubane water oxidation catalyst. *ACS Catal.* **11**, 13320–13329 (2021).
2. E. C. M. Tse *et al.*, Proton transfer dynamics control the mechanism of O_2 reduction by a non-precious metal electrocatalyst. *Nat. Mater.* **15**, 754–759 (2016).
3. P. Gayen, S. Saha, X. Liu, K. Sharma, V. K. Ramani, High-performance AEM unitized regenerative fuel cell using Pt-pyrochlore as bifunctional oxygen electrocatalyst. *Proc. Natl. Acad. Sci. U.S.A.* **118**, e2107205118 (2021).
4. A. Mehmood *et al.*, High loading of single atomic iron sites in Fe–NC oxygen reduction catalysts for proton exchange membrane fuel cells. *Nat. Catal.* **5**, 311–323 (2022).
5. M. Dan *et al.*, Strategies and challenges on selective electrochemical hydrogen peroxide production: Catalyst and reaction medium design. *Chem Catal.* **2**, 1919–1960 (2022).
6. N. Zhang *et al.*, High-density planar-like Fe_2N_6 structure catalyzes efficient oxygen reduction. *Matter* **3**, 509–521 (2020).
7. B. Mondal *et al.*, Elucidation of factors that govern the $2e^-/2h^+$ vs $4e^-/4h^+$ selectivity of water oxidation by a cobalt corrole. *J. Am. Chem. Soc.* **142**, 21040–21049 (2020).
8. Z. Lu *et al.*, An isolated zinc–cobalt atomic pair for highly active and durable oxygen reduction. *Angew. Chem. Int. Ed. Engl.* **58**, 2622–2626 (2019).
9. J. Li *et al.*, Identification of durable and non-durable FeN_4 sites in Fe–N–C materials for proton exchange membrane fuel cells. *Nat. Catal.* **4**, 10–19 (2021).
10. J. Yan *et al.*, Breaking platinum nanoparticles to single-atomic Pt-C_4 Co-catalysts for enhanced solar-to-hydrogen conversion. *Angew. Chem. Int. Ed. Engl.* **60**, 2541–2547 (2021).
11. Y. Yan *et al.*, Robust wrinkled MoS_2/N-C bifunctional electrocatalysts interfaced with single Fe atoms for wearable zinc-air batteries. *Proc. Natl. Acad. Sci. U.S.A.* **118**, e2110036118 (2021).
12. J.-C. Dong *et al.*, In situ Raman spectroscopic evidence for oxygen reduction reaction intermediates at platinum single-crystal surfaces. *Nat. Energy* **4**, 60–67 (2019).
13. C. Dong *et al.*, Dual-functional single-atomic Mo/Fe clusters–decorated C_3N_5 via three electron-pathway in oxygen reduction reaction for tandemly removing contaminants from water. *Proc. Natl. Acad. Sci. U.S.A.* **120**, e2305883120 (2023).
14. H. T. Chung *et al.*, Direct atomic-level insight into the active sites of a high-performance PGM-free ORR catalyst. *Science* **357**, 479–484 (2017).
15. L. Yang *et al.*, Unveiling the high-activity origin of single-atom iron catalysts for oxygen reduction reaction. *Proc. Natl. Acad. Sci. U.S.A.* **115**, 6626–6631 (2018).
16. A. J. Martín, S. Mitchell, C. Mondelli, S. Jaydev, J. Pérez-Ramírez, Unifying views on catalyst deactivation. *Nat. Catal.* **5**, 854–866 (2022).
17. W. Guo, Z. Wang, X. Wang, Y. Wu, General design concept for single-atom catalysts toward heterogeneous catalysis. *Adv. Mater.* **33**, 2004287 (2021).
18. D. Yu *et al.*, Dual-sites coordination engineering of single atom catalysts for flexible metal–air batteries. *Adv. Energy Mater.* **11**, 2101242 (2021).
19. Z. Qiao *et al.*, Atomically dispersed single iron sites for promoting Pt and Pt_3Co fuel cell catalysts: Performance and durability improvements. *Energy Environ. Sci.* **14**, 4948–4960 (2021).
20. S. Huang *et al.*, Sublayer stable Fe dopant in porous pd metallene boosts oxygen reduction reaction. *ACS Nano* **16**, 522–532 (2022).
21. X. Wu *et al.*, Sublayer-enhanced atomic sites of single atom catalysts through in situ atomization of metal oxide nanoparticles. *Energy Environ. Sci.* **15**, 1183–1191 (2022).
22. X. Liang *et al.*, Two types of single-atom FeN_4 and FeN_5 electrocatalytic active centers on N-doped carbon driving high performance of the SA-Fe-NC oxygen reduction reaction catalyst. *Chem. Mater.* **33**, 5542–5554 (2021).
23. A. Kumar, K. Sun, X. Duan, S. Tian, X. Sun, Construction of dual-atom Fe via face-to-face assembly of molecular phthalocyanine for superior oxygen reduction reaction. *Chem. Mater.* **34**, 5598–5606 (2022).
24. C. Hu *et al.*, Near- and long-range electronic modulation of single metal sites to boost CO_2 electrocatalytic reduction. *Adv. Mater.* **35**, 2209298 (2023).
25. Y. Liu *et al.*, Tuning the spin state of the iron center by bridge-bonded Fe-O-Ti ligands for enhanced oxygen reduction. *Angew. Chem. Int. Ed. Engl.* **61**, e202117617 (2022).
26. K. Chen *et al.*, Iron phthalocyanine with coordination induced electronic localization to boost oxygen reduction reaction. *Nat. Commun.* **11**, 4173 (2020).
27. X. Tan *et al.*, Square-pyramidal Fe-N_4 with defect-modulated O-coordination: Two-tier electronic structure fine-tuning for enhanced oxygen reduction. *Chem Catal.* **2**, 816–835 (2022).
28. S. Bhunia, A. Ghatak, A. Dey, Second sphere effects on oxygen reduction and peroxide activation by mononuclear iron porphyrins and related systems. *Chem. Rev.* **122**, 12370–12426 (2022).
29. J. P. Collman, Y. Ha, R. Guilard, M. A. Lopez, Chemistry of a cofacial dirhodium diporphyrin: Synthesis and reactivity of Rh_2DPB. *Inorg. Chem.* **32**, 1788–1794 (1993).
30. S. Tang *et al.*, Realizing a not-strong-not-weak polarization electric field in single-atom catalysts sandwiched by boron nitride and graphene sheets for efficient nitrogen fixation. *J. Am. Chem. Soc.* **142**, 19308–19315 (2020).
31. J. Büker *et al.*, Synthesis of Cu single atoms supported on mesoporous graphitic carbon nitride and their application in liquid-phase aerobic oxidation of cyclohexene. *ACS Catal.* **11**, 7863–7875 (2021).
32. S. Ji *et al.*, Matching the kinetics of natural enzymes with a single-atom iron nanozyme. *Nat. Catal.* **4**, 407–417 (2021).
33. Z. Li *et al.*, Iridium single-atom catalyst on nitrogen-doped carbon for formic acid oxidation synthesized using a general host–guest strategy. *Nat. Chem.* **12**, 764–772 (2020).
34. L. Wang *et al.*, Periodic one-dimensional single-atom arrays. *J. Am. Chem. Soc.* **144**, 15999–16005 (2022).
35. L. Bai, C.-S. Hsu, D. T. L. Alexander, H. M. Chen, X. Hu, Double-atom catalysts as a molecular platform for heterogeneous oxygen evolution electrocatalysis. *Nat. Energy* **6**, 1054–1066 (2021).
36. L. Cao *et al.*, Identification of single-atom active sites in carbon-based cobalt catalysts during electrocatalytic hydrogen evolution. *Nat. Catal.* **2**, 134–141 (2019).
37. Q. Zhao *et al.*, Approaching a high-rate and sustainable production of hydrogen peroxide: Oxygen reduction on Co–N–C single-atom electrocatalysts in simulated seawater. *Energy Environ. Sci.* **14**, 5444–5456 (2021).
38. Y. Xiong *et al.*, Single-atom Rh/N-doped carbon electrocatalyst for formic acid oxidation. *Nat. Nanotechnol.* **15**, 390–397 (2020).
39. H. Zhang *et al.*, A graphene-supported single-atom FeN_5 catalytic site for efficient electrochemical CO_2 reduction. *Angew. Chem. Int. Ed. Engl.* **58**, 14871–14876 (2019).
40. J.-R. Huang *et al.*, Single-product faradaic efficiency for electrocatalytic of CO_2 to CO at current density larger than 1.2 A cm^{-2} in neutral aqueous solution by a single-atom nanozyme. *Angew. Chem. Int. Ed. Engl.* **61**, e202210985 (2022).

41. Y. Wu *et al.*, Boosting CO_2 electroreduction over a cadmium single-atom catalyst by tuning of the axial coordination structure. *Angew. Chem. Int. Ed. Engl.* **60**, 20803–20810 (2021).
42. Y. Sun *et al.*, Biomimetic FeMo(Se, Te) as joint electron pool promoting nitrogen electrofixation. *Angew. Chem. Int. Ed. Engl.* **61**, e202115198 (2022).
43. Y. Wen *et al.*, Isolation of metalloid boron atoms in intermetallic carbide boosts the catalytic selectivity for electrocatalytic N_2 fixation. *Adv. Energy Mater.* **11**, 2102138 (2021).
44. Z. Wang *et al.*, Cation-tuning induced d-band center modulation on Co-based spinel oxide for oxygen reduction/evolution reaction. *Angew. Chem. Int. Ed. Engl.* **61**, e202114696 (2022).
45. K. Sun *et al.*, Nature-inspired design of molybdenum–selenium dual-single-atom electrocatalysts for CO_2 reduction. *Adv. Mater.* **34**, 2206478 (2022).
46. J. Fu, K. Jiang, X. Qiu, J. Yu, M. Liu, Product selectivity of photocatalytic CO_2 reduction reactions. *Mater. Today* **32**, 222–243 (2020).
47. B.-A. Lu *et al.*, Structurally disordered phosphorus-doped Pt as a highly active electrocatalyst for an oxygen reduction reaction. *ACS Catal.* **11**, 355–363 (2021).
48. J. Zheng *et al.*, Preferred orientation of TiN coatings enables stable zinc anodes. *ACS Energy Lett.* **7**, 197–203 (2022).
49. J. Zhang, Z. Zhao, Z. Xia, L. Dai, A metal-free bifunctional electrocatalyst for oxygen reduction and oxygen evolution reactions. *Nat. Nanotechnol.* **10**, 444–452 (2015).